Plasma-assisted combustion with nanosecond discharges. Part I: discharge effects characterization in the burnt gases of a lean flame

Nicolas Minesi, Victorien Blanchard, Erwan Pannier, Gabi Daniel Stancu, Christophe O Laux

▶ To cite this version:

Nicolas Minesi, Victorien Blanchard, Erwan Pannier, Gabi Daniel Stancu, Christophe O Laux. Plasma-assisted combustion with nanosecond discharges. Part I: discharge effects characterization in the burnt gases of a lean flame. Plasma Sources Science and Technology, 2022, 10.1088/1361-6595/ac5cd4 . hal-03607157

HAL Id: hal-03607157
https://hal.science/hal-03607157

Submitted on 12 Mar 2022

Plasma Sources Science and Technology

ACCEPTED MANUSCRIPT

Plasma-assisted combustion with nanosecond discharges. Part I: discharge effects characterization in the burnt gases of a lean flame

To cite this article before publication: Nicolas Minesi *et al* 2022 *Plasma Sources Sci. Technol.* in press https://doi.org/10.1088/1361-6595/ac5cd4

Manuscript version: Accepted Manuscript

Accepted Manuscript is “the version of the article accepted for publication including all changes made as a result of the peer review process, and which may also include the addition to the article by IOP Publishing of a header, an article ID, a cover sheet and/or an ‘Accepted Manuscript’ watermark, but excluding any other editing, typesetting or other changes made by IOP Publishing and/or its licensors”

This Accepted Manuscript is **© 2022 IOP Publishing Ltd**.

During the embargo period (the 12 month period from the publication of the Version of Record of this article), the Accepted Manuscript is fully protected by copyright and cannot be reused or reposted elsewhere.
As the Version of Record of this article is going to be / has been published on a subscription basis, this Accepted Manuscript is available for reuse under a CC BY-NC-ND 3.0 licence after the 12 month embargo period.

After the embargo period, everyone is permitted to use copy and redistribute this article for non-commercial purposes only, provided that they adhere to all the terms of the licence https://creativecommons.org/licences/by-nc-nd/3.0

Although reasonable endeavours have been taken to obtain all necessary permissions from third parties to include their copyrighted content within this article, their full citation and copyright line may not be present in this Accepted Manuscript version. Before using any content from this article, please refer to the Version of Record on IOPscience once published for full citation and copyright details, as permissions will likely be required. All third party content is fully copyright protected, unless specifically stated otherwise in the figure caption in the Version of Record.

View the article online for updates and enhancements.

This content was downloaded from IP address 131.179.52.199 on 12/03/2022 at 00:55

Plasma-assisted combustion with nanosecond discharges. Part I: discharge effects characterization in the burnt gases of a lean flame

N. Q. Minesi, V. P. Blanchard, E. Pannier, G. D. Stancu, C. O. Laux

EM2C, CNRS, CentraleSupélec, Université Paris Saclay, 3 Rue Joliot-Curie, 91190 Gif-sur-Yvette, France

Keywords: flame stabilization, lean premixed combustion, quantitative OES, Stark broadening, CH_4, NRP discharges,

The prediction of a flame response to plasma assistance requires extensive knowledge of discharge-induced plasma kinetics. Detailed studies of nanosecond discharges are common in N_2/O_2 and fresh combustible mixtures but are still lacking in burnt gases. To fill this gap, we define a combustion reference test case and investigate the effects of Nanosecond Repetitively Pulsed (NRP) discharges placed in the recirculation zone of a lean (Φ = 0.8) CH_4-air bluff-body stabilized flame at atmospheric pressure. In this zone, the plasma discharge is created in a mixture of burnt gases. Quantitative Optical Emission Spectroscopy (OES), coupled with measurements of electrical energy deposition, is performed to provide temporally (2 ns) and spatially (0.5 mm) resolved evolutions of the temperatures and concentrations of $N_2(B)$, $N_2(C)$, $N_2^+(B)$, OH(A), NH(A), and CN(B) in the discharge. At steady state, the 10-ns pulses deposit 1.8 mJ at a repetition frequency of 20 kHz. Spatially resolved temperature profiles are measured during the discharge along the interelectrode gap. The temperature variations are more pronounced near the electrodes than in the middle of the gap. On average, the gas temperature increases by approximately 550 K. The heat release corresponds to about 20% of the total deposited electric energy. The electron number density, measured by Stark broadening of H_α, increases up to about 10^{16} cm^{-3}. These characteristics allow to classify the discharge as a non-equilibrium NRP spark, as opposed to the thermal NRP spark where the temperature can reach 40,000 K and the degree of ionization is close to 100%. These measurements will serve (i) as a reference for future studies in the Mini-PAC burner at the same conditions, (ii) to test discharge kinetic models, and (iii) to derive a simplified model of plasma-assisted combustion, which will be presented in companion paper.

1. Introduction

Plasma-Assisted Combustion (PAC) has triggered scientific attention for decades and several studies reviewed the experimental and numerical works performed on the subject [1–4]. In a review of PAC experiments performed in a wide range of pressures (0.01 – 10 atm) and temperatures (300 – 2000 K), Starikovskaia [1] stressed that kinetic models can predict the shortening of autoignition delay times but fail by several orders of magnitude to predict the absolute concentrations of radicals and active species. Thus, as also suggested by Ju and Sun [2], there is a need for the development and validation of PAC kinetics.

It was shown in various mixtures and conditions that atomic oxygen plays a dominant role in PAC [2]. Popov [3] summarized the recent advances in PAC models, and notably showed that atomic oxygen is more effective than electronically excited O_2 or vibrationally excited species. Thus, for effective plasma assistance, Popov recommended loading energy into the electronic states of N_2, which then induce oxygen dissociation via quenching reactions. This energy loading can be efficiently achieved with a reduced electric field E/N = 100 – 500 Td. Thus, an efficient PAC system requires high reduced electric fields, but practical considerations also impose low average power sources. Applied at frequencies from 10 to 100 kHz, Nanosecond Repetitively Pulsed (NRP) discharges meet these two criteria by reaching several kV during ~10 ns, while keeping the average electric power near tens of watts. For these reasons, NRP discharges are a promising tool for PAC applications.

In the literature on flame stabilization, NRP discharges are applied at different locations in the burners, either in the fresh gases or the burnt gases. In fresh gases, applying the discharge in a non-premixed CH_4 turbulent flame significantly reduced its detachment height [5]. Mao *et al.* [6] also recently demonstrated that, in methane/N_2 mixtures, significant heat release and H_2 formation was observed and attributed to N_2 electronic excited states quenching. In n-dodecane/O_2/N_2 mixtures, Zhong *et al.* [7] showed that $N_2(A)$ and $N_2(a')$ accelerated the oxidation of dodecane by dissociative quenching of N_2^* with O_2 forming O, $O(^1D)$, and $O(^1S)$. In CH_4/air, Kim *et al.* [8] showed that NRP discharges extend the flame lean blow-off limit via the formation of a cool flame and that the stabilization effect was mainly driven by CO and H_2 formation. In the study Shcherbanev et al. [9], NRP discharges initiated in natural gas anchored a 50-kW flame in various conditions. Progress has also been achieved in plasma-assisted ignition by modulating the repetition frequency of the NRP [10] discharges.

As mentioned before, stabilization can also be obtained when the discharge is applied in recirculating burnt gases. Demonstrations were conducted at the EM2C laboratory in the so-called Mini-PAC bluff-body burner [11] and the MultiPoint swirled burner [12], showing that NRP discharges applied in the recirculation zone reduced the lean extinction limit of methane/air and propane/air flames. A more recent study performed using methane, liquid heptane, and liquid dodecane also showed that the lean extinction limit can be extended by applying NRP discharges in the outer recirculation zone [13]. In these three examples [11–13], the activated burnt gases recirculate and mix with fresh gases to promote stabilization [14]. NRP discharges have also been applied to suppress thermoacoustic instabilities [13,15], and again the discharges were applied in the burnt gases.

In recent years, kinetic models have been developed to predict the chemical and thermal effects of nanosecond discharges in air [16–18] or in combustible mixtures [3]. An issue for complete numerical simulations of practical applications is the difference between plasma timescales (picoseconds to nanoseconds) and combustion timescales (nanoseconds to milliseconds) [4]. A simplified model of active species and heat production was successfully developed for NRP discharges in fresh methane/air mixtures [19] and successfully applied to simulate ignition [20]. However, this model must be extended to burnt gas mixtures where the main species are no longer CH_4 and air, but CO_2, H_2O, and N_2 (and O_2 in lean mixtures). The present study intends to fill this gap by providing data for the experimental validation of kinetic models and for the derivation of a simplified plasma-assisted combustion model in burnt gases (companion article, Part II).

The stabilization performance greatly depends on the kind of NRP discharge. There exist four types as described in Table 1: corona, glow, spark, and thermal sparks [21,22]. Corona and glow NRP discharges are non-equilibrium plasmas and do not appreciably heat the gas [23]. Sparks also produce non-equilibrium plasmas but the gas temperature increases by a few 1000 K through the ultrafast heating mechanism [16,24]. Finally, thermal sparks present a fast transit to equilibrium due to electron-ion collisions [25] and reach full ionization and equilibrium temperatures around 40,000 K [22]. These thermal sparks produce a plasma that resembles those in laser-driven discharges with similar electron number density and temperatures [26]. Note that the total energy deposition is not an accurate criterion to differentiate the NRP regimes [22].

Table 1 Typical parameters of NRP corona, glow [23]**, spark** [24,27] **and thermal spark** [22,25] **discharges at ambient pressure. The deposited electrical energy is given for cases where the discharge dimension is of the order of a millimeter..**

	Non-equilibrium			**Equilibrium**
Regime	Corona	Glow	Spark	Thermal spark
Deposited Energy	<10 µJ	~10 µJ	~1 mJ	~1 mJ
Dominant Emission	Molecular (N_2)	Molecular (N_2)	Molecular (N_2) Atomic (O)	Atomic (N, O) Ionic (N^+, O^+) Continuum
Maximum electron Number Density	<10^{13} cm^{-3}	10^{13} cm^{-3}	10^{15}-10^{16} cm^{-3}	10^{19} cm^{-3}
Temperature Increase	Negligible	<200 K	~1000 K	~40,000 K

In most PAC experiments with NRP discharges, beneficial effects are observed when the energy of the pulses is of the order of 1 mJ or above, i.e. in the non-equilibrium regime, which produces high radical densities with limited gas heating [2,11,12,28–30], or in the thermal spark regime, which provides full ionization and extreme gas temperatures. To our knowledge, the performance of NRP thermal sparks in PAC has not been compared to other types of non-equilibrium NRP discharges.

In this work, we will characterize the NRP discharge and the production of heat and active species in the Mini-PAC burner employing a bluff-body stabilized lean methane-air flame configuration, using quantitative Optical Emission Spectroscopy (OES) and electrical diagnostics. In Section 2, we present the Mini-PAC burner and the OES setup. Section 3 describes the electrical characterization of the NRP discharges. Measurements by OES are presented in the three following sections: the gas temperature in Section 4, the electron number density in Section 5, the quantification of the various excited states produced by the discharge is given then in Section 6, and finally conclusions are provided in Section 7. The measurements presented in this work are tabulated in the supplementary material.

2. Experimental setup

This section describes the Mini-PAC burner setup ("Mini Plasma-Assisted Combustion" burner). The burner is similar to the configuration of Refs. [11,31], with the difference that the present experiments are conducted with methane instead of propane. The pressure is 1 atm. The schematic of the burner exit is presented in Figure 1. The internal diameter of the burner injection tube is 16 mm, and the bluff-body diameter is 10 mm. The Reynolds number, based on the hydraulic diameter of the burner outlet, is about 16,000, indicating that the flow is turbulent.

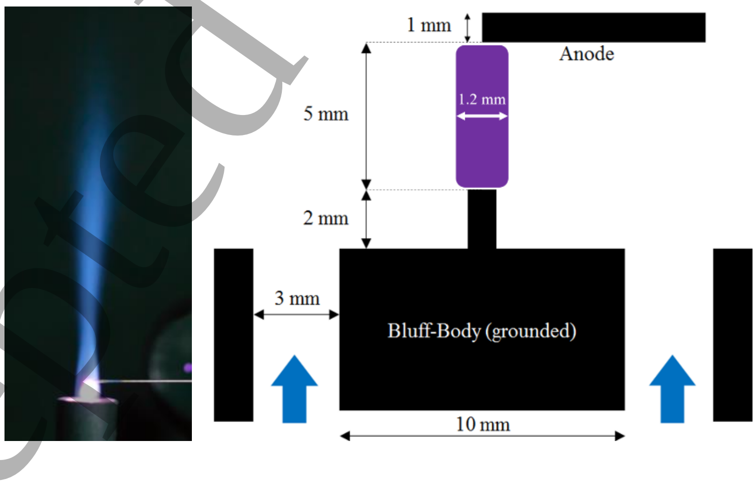

Figure 1 Left: Picture of the plasma-stabilized flame (Hasselblad H3DII-31 digital camera) [32]**. The CCD is overexposed in the plasma region. Right: Schematic of the Mini-PAC burner outlet and electrode configuration** [33]**. The plasma is represented in purple. The effect of plasma assistance on the flame topology is shown in the video provided as supplementary material.**

The NRP discharges are initiated in the recirculation zone, which is mainly composed of burnt gases. High-voltage nanosecond pulses of 15 ns duration, produced by an FID pulser (model FPG 30-100MC4K), are applied across a 5-mm gap, between a horizontal tungsten electrode (positively biased) and a vertical tungsten electrode (see Figure 1). The vertical electrode is mounted onto the grounded bluff-body. The diameter of the electrodes is 1 mm. The output of the high-voltage pulse generator is connected to the anode by a 75-Ω coaxial cable (Alphawire 9011a).

The experimental setup for optical and electrical diagnostics is presented in Figure 2. For the OES measurements, the discharge emission is focused on the slit of a 50-cm monochromator (Acton SP2500i) via two 10-cm plano-convex lenses. The monochromator is coupled with an ICCD camera (PI-MAX 2, Princeton Instruments) with a minimal gate exposure of 2 ns. The diameter of the discharge, measured from the total emission, is 1.2-mm (FWHM of the measured Gaussian profile with an uncertainty of 50 µm). Absolute intensity calibration of the emission spectra is performed with an integrating sphere (OL455, Gooch and Housego). A bandpass filter in the 250 – 400 nm range (Melles Griot – 03 FCG 177) is used to minimize the effect of stray light in the spectrometer during the experiments in the UV. For the visible and IR spectra, a 550-nm long-pass filter is used (Melles Griot – OG550 – 03 FCG 087). The electrical characteristics of the NRP discharges are monitored on an oscilloscope (HDO 6104, Teledyne Lecroy) using voltage (PPE 20kV, Teledyne Lecroy) and current (Current Monitor Model 6585, Pearson Electronics) probes.

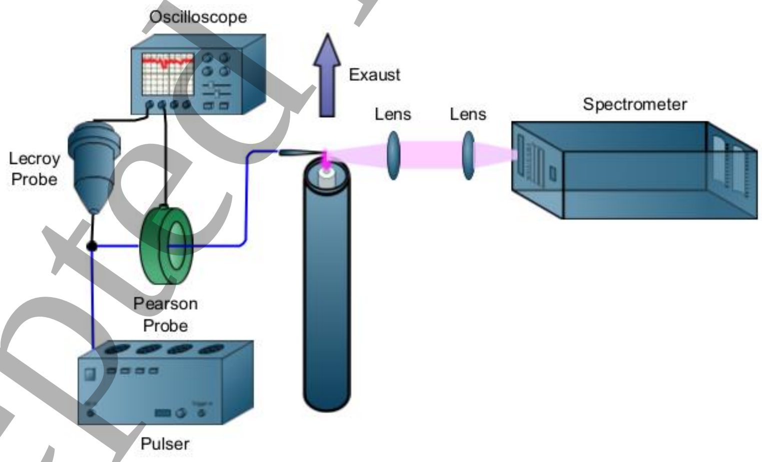

Figure 2 Experimental setup with OES and electrical measurements.

All results are obtained at atmospheric pressure in a lean methane-air flame (Φ = 0.8) under the following experimental conditions (which will be referred to as the “PASTEC” conditions):

- Air flowrate: $\dot{Q}_{air}$ = 16 $m^3 \cdot h^{-1}$ ($\dot{m}_{air}$ = 5.75 $g \cdot s^{-1}$)

- CH$_4$ flowrate: $\dot{Q}_{CH_4}$ = 1.34 m^3·h^{-1} ($\dot{m}_{CH4}$ = 0.27 g·s^{-1})
- Incident pulse duration: 15 ± 1 ns
- Maximum voltage at the electrode: 6 kV – see Figure 3
- Voltage amplitude of the incident pulses: 3.5 kV – see Appendix
- Discharge repetition rate: 20 kHz

The theoretical flame thermal power is 13.3 kW if methane is completely burnt. However, without plasma assistance, most of the methane is not burnt and the flame is confined to the recirculation zone behind the bluff body, see Chapter 8 of [32]. The deposited energy at steady state is about 1.8 mJ per pulse (see Section 3), approximately 0.3% of the flame thermal power. With plasma, a stable and elongated flame is obtained, see Figure 1. A video with and without plasma assistance is available in the Supplementary material. As will be shown later, the plasma produced by the discharge is a non-equilibrium NRP spark [21] ($n_{e,\,max}$ = 10^{16} cm^{-3} and T_{max} = 3300 K). All measurements presented in this article are performed in the steady-state pulsing regime.

3. Energy deposited by NRP discharges

The following electrical measurements are performed at the electrodes (the distance between the electrical probes and the electrode is less than 5 cm). The voltage, current, and deposited energy measured at the anode at steady state are shown in Figure 3. The traces are averaged (over at least 1000 measurements) and the standard deviations of the current and voltage are below 7%. Once integrated, these variations lead to a 12% statistical fluctuation (1σ) of the measured energy. We start the time reference t = 0 ns when the current is above 1 A. The first peak of current is measured at t = 11 ns. After this instant, the abrupt fall of both current and voltage marks the end of the energy deposition. The OES and electrical measurements are synchronized by matching the peaks of the OES signal and of the current at t = 11 ns [24]. By 30 ns, approximately 1.50 mJ are deposited. Another method to measure the deposited energy consists in placing the voltage and current probes halfway of the coaxial cable, as presented in the Appendix.

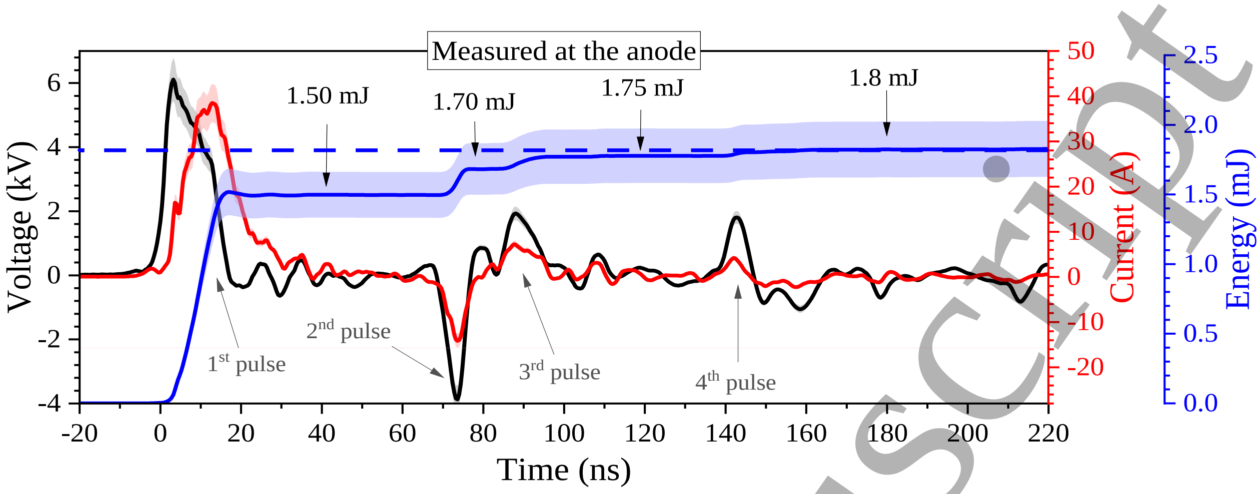

Figure 3 Voltage (black) and current (red) measured at the anode. The energy deposited in the plasma is obtained by integrating the product of the voltage and the current (the light blue swath indicates the standard deviation). PASTEC conditions: Φ = 0.8, *f* = 20 kHz, E^p = 1.8 mJ.

At *t* = 70 ns, a reflected voltage pulse of -4 kV is measured at the electrode, rapidly followed by a second reflected pulse of +2 kV at *t* = 90 ns. The two pulses between 70 and 100 ns deposit approximately 0.25mJ. At *t* = 140 ns, 0.05 mJ are deposited by a 4th pulse (+2 kV). The 3rd pulse is related to the internal electronics of the pulser, which is known for generating additional pulses [24]. The 2nd and 4th pulses are reflections of the initial pulse arising due to the impedance mismatch of the coaxial cable with the plasma or the pulser. Their polarities alternate (1st: positive, 2nd: negative, 4th: positive) which indicates that the pulser impedance is much smaller than the cable impedance (75 Ω). With these four pulses, a total energy of 1.8 mJ is thus deposited within 150 ns. Therefore, the ratio of the plasma electric power (36 W) and flame maximal thermal power (13.3 kW) is equal to 0.3%.

The discharge can be approximated by a cylinder of 0.6±0.05 mm (radius) by 5±0.05 mm (height), as measured by imaging, which gives an initial volume of $V = 5.6\pm0.5\times10^{-3}$ cm^3. Thus, the energy density by the end of the discharge is 0.34 J·cm^{-3}. With the initial density of the gas $n = 2.8\times10^{18}$ cm^{-3} (see Section 4), the energy deposited per molecule is 0.74 eV·molecule^{-1}, which is typical for non-equilibrium sparks [9,34,35].

4. Gas temperature

In this section, the emission of the second positive system of N_2 is measured using a 2400-gr/mm grating and an entrance slit of 50 µm (spectral instrumental broadening HWHM of 0.050 nm). The measurements are spatially resolved along the interelectrode gap. The N_2(C-B) (second positive system) emission is fitted using the line-by-line radiation code Specair [36,37] as shown in Figure 4, which compares a representative experimental spectrum with the best fit and two other spectra calculated at $T_{rot} = T_{fit} \pm 200$ K. This uncertainty is likely due to the variations of the excited state densities and temperature along the line-of-sight. However, the measured values are dominated by the emission of the hot plasma core, which produces most of the emission [37]. As shown in Table 1, the identification of the NRP discharge type can also be aided by measuring the temperature increase.

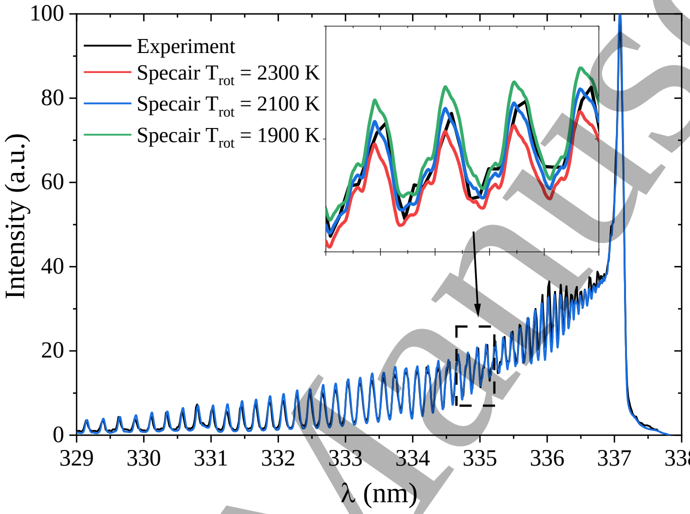

Figure 4 Sensitivity of the N_2(C-B) (0-0) spectrum to the rotational temperature. The measurement (in black) is performed under the PASTEC conditions (Φ = 0.8, f = 20 kHz, E^p= 1.8 mJ), z = 4.75 mm (anode), and t = 10 ns. The best fit, shown in blue, is obtained for T_{rot} = 2100 K.

The temporal evolution of the N_2(C) rotational temperature along the inter-electrode axis after discharge breakdown is shown in Figure 5 (bottom). During the first nanoseconds, the temperature is higher in the middle of the interelectrode gap than at the electrodes. From 0 to 18 ns, the temperature in the middle of the gap increases mildly from about 3000 to 3300 K. In contrast, near the electrodes, the temperature increases much more, from 2000 to about 3000 K. Note that the temperature does not significantly change from 0 to 5 ns. The spatial average of the temperature increase is equal to ΔT = 550 K. The dependence of the temperature increase with position suggests that the energy deposition *is not* homogeneous along the interelectrode gap. However, it appears that after the discharge the temperature becomes close to homogeneous across the entire gap. In the present case, this latter aspect is expected to simplify the assumptions on the plasma temperature distribution that are necessary in plasma-assisted combustion modeling.

The temperatures measured at the beginning of the second pulse ($t \approx 70$ ns) are close to the temperatures measured at the end of the 1st pulse (see Figure 5 top). This indicates that no significant heating occurred during the 20 – 70 ns interval (where the $N_2(C)$ emission is too weak to be measured). During the 2nd pulse, the temperature increases by nearly 800 K near the anode but only by 300 K near the cathode. However, it remains constant in the middle of the gap (z = 2.25 mm). During the 3rd and 4th pulses, the $N_2(C)$ emission is not intense enough to determine the temperature evolution.

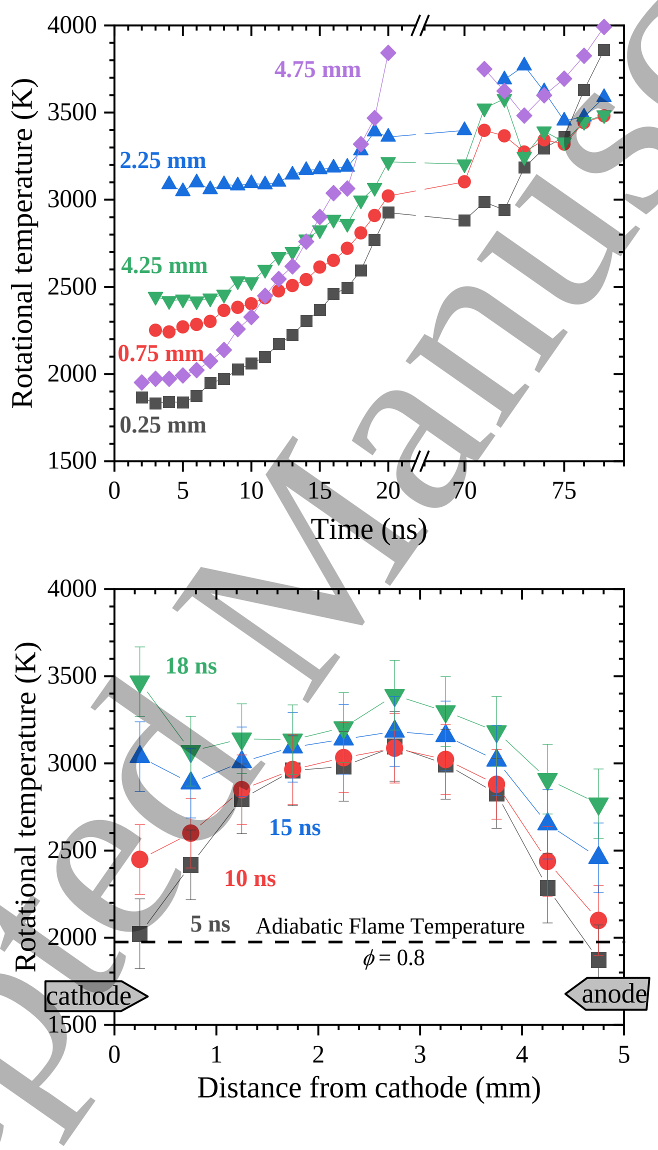

Figure 5 *Top*: Evolution of the rotational temperature along the interelectrode gap. The temperature measurements at *t* = 70 – 80 ns are obtained with the 2nd pulse. *Bottom*: Map of the rotational temperature along the interelectrode gap at *t* = 5, 10, 15, and 18 ns. The temperature distribution at *t* = 0 ns is similar to that at *t* = 5 ns. The adiabatic flame temperature at Φ = 0.8 (1979 K) is given for comparison (dashed line). Interelectrode distance: 5 mm. PASTEC conditions: Φ = 0.8, *f* = 20 kHz, E^p = 1.8 mJ.

It is important to note that the rotational temperature T_{rot} of $N_2(C)$ is close to the translation temperature T_{trans}. This can be understood because at E/N > 120 Td, $N_2(C)$ is primarily populated by electron impact [38]. This reaction maps the rotational distribution of $N_2(X)$, which is in equilibrium with the gas temperature at the considered conditions [24,38]. The nascent rotational distribution of $N_2(C)$ is therefore a Boltzmann distribution at $T_{rot} = \left(B_{e,C}/B_{e,X}\right)T_{trans}$ [24,39], where $B_{e,i}$ is the rotational constant of the electronic state *i*. Eventually, T_{rot} relaxes to T_{trans} via rotational-translational relaxation. Thus, the difference between T_{rot} and T_{trans} is at most 10% at initial times because the $B_{e,C}/B_{e,X}$ ratio is equal to 0.9 [24] and we assume $T_{rot} = T_{trans}$ in the rest of this work.

The initial temperature of 3000 K in the middle of the gap results from the gas heating of previous discharges. Near the electrodes, the temperature at $t < 2$ ns is about 2000 K, which corresponds to the adiabatic temperature of a lean flame at $\Phi = 0.8$. During the period between two consecutive discharges, the gas hydrodynamic effects following nanosecond discharges are responsible for the entrance of gas at 2000 K into the near-electrode space. To our knowledge, this phenomenon was first observed in 1952 [40], with further study in subsequent decades [41,42]. The hydrodynamics of nanosecond discharges has also recently received particular attention [43–46]. Thanks to time-resolved radial measurements of the pressure in the afterglow of a nanosecond discharge in air [47] and numerical simulations [48], the baroclinic torque was shown to be responsible for the vorticity generation and the entrance of cooler gases in the interelectrode gap. The cooling of the near-electrode region is, therefore, consistent with the hydrodynamic effect following the discharge.

In this paragraph, our objective is to quantify the energy value, $\Delta E_{heating}$, which corresponds to the ultrafast heating observed during our experiments over the first 20 ns. As stated previously, the temperature increase measured here represents the variation of the translational and rotational temperatures. These temperatures are equilibrated, and we have $\Delta E_{trans} + \Delta E_{rot} = NV\ 5/2\ k_B \Delta T$ because the mixture is mainly comprised of diatomic and linear triatomic molecules. Moreover, during the first 100 ns of the discharge, vibrational-translational energy exchange is negligible [24,39]. We thus have:

$$\Delta E_{heating} \approx \Delta E_{trans} + \Delta E_{rot} \approx NV\frac{5}{2}k_B\ \Delta T \qquad \text{Eq. 1}$$

Using the time-resolved temperature measurements shown in Figure 5, we can infer the fraction of the discharge energy dissipated into ultrafast gas heating. We recall that we can approximate the discharge by a cylinder with a volume of $V = 5.6 \pm 0.5 \times 10^{-3}$ cm^3 in which the average temperature is approximately 2610 K at $t = 0$ ns, and 3160 K at $t = 18$ ns. Given the low noise and smooth variations observed in Figure 5, the uncertainty on the temperature measurement is systematic; thus $\Delta T = 550 \pm 200$ K.

Because the discharge is isochoric, the gas number density is constant, $N = 2.8 \pm 0.2 \times 10^{18}$ cm^{-3}. From Eq. 1, the energy required to heat the discharge volume during the first 20 ns of the discharge is estimated to be 300±110 µJ. The deposited energy in the first 20 ns is 1.5 mJ. Thus, we estimate that 20% of the deposited energy is converted to ultrafast heating. Propagating the uncertainties, we find that the actual percentage lies between 12% and 28%. The average value of 20% is similar to the value measured for NRP discharges in preheated air at 1500 K (Rusterholtz *et al.* [24]). The reduced electric field[1] of the first pulse is at most 430 Td. It was predicted [18,49,50] by numerical simulations in air that 20±10% of the deposited energy is converted to heat for E/N = 100 - 500 Td, which is comparable with the value of about 20% measured here in the burnt gases.

Table 2 Mole fractions in an equilibrium mixture of CH_4 – air ($\Phi = 0.8$) at 2000 and 3000 K calculated with the CEA NASA code [51]**. The γ_{pert} factors are used in Section 5 to calculate the Van der Waals broadening of H_α and are taken from Table A3-A5 of Ref.** [22]**. All CH_4 is consumed at 2000 K, as expected in the recirculation zone where only burnt gases and unconsumed O_2 molecules remain.**

Species	N_2	H_2O	CO_2	O_2	CO	H_2	H	NO	OH
Mole fraction at 2000 K	71.8%	15.3%	7.7%	3.7%	0.1%	0.0%	0.0%	0.3%	0.2%
Mole fraction at 3000 K	66.0%	9.4%	2.8%	4.3%	4.4%	2.0%	2.2%	2.0%	3.7%
γ_{pert} (nm)	2.9	2.7	3.4	5.2	3.1	3.6	-	5.9	-

5. Electron number density

The measurement of the electron number density also allows to characterize the NRP discharge regime, see Table 1. At atmospheric conditions, the typical electron number density will be $<10^{13}$ cm^{-3} for coronas, $\sim 10^{13}$ cm^{-3} for glows, $\sim 10^{15} - 10^{16}$ cm^{-3} for sparks and $\sim 10^{19}$ cm^{-3} for thermal sparks [21,22]. Here, the electron number density is measured from the Stark broadening of the H_α line at 656 nm. As described in Refs. [22,37,52], the total Half-Width at Half Maximum (HWHM) of H_α is the sum of several broadening mechanisms: instrumental, Doppler, resonance, natural, Van der Waals, and Stark.

The instrumental HWHM measured with a HeNe laser at λ = 632.8 nm is approximately equal to 0.035 nm. Natural broadening is negligible. The Doppler HWHM varies slowly with temperature ($\sqrt{T}$) from 0.011 nm to 0.013 nm [22]. For simplicity, the Doppler HWHM will be considered constant and equal to 0.012 nm.

---

[1] We took $N = 2.8 \cdot 10^{18}$ cm^{-3}, d = 5 mm, and $\Delta V = 6$ kV to get $E/N = 4.3 \cdot 10^{-15}$ $V \cdot cm^2$ = 430 Td.

The number density of atomic hydrogen is estimated to be below 10^{15} cm^{-3} according to the equilibrium composition given in Table 2, resulting in negligible resonance broadening (< 0.001 nm). This low number density of H atoms was also observed experimentally in a low pressure flame [53].

The Van der Waals HWHM is obtained by summing the contributions of the perturbers, *pert*, in the sum of Eq. 2, where p [atm] is the pressure, T_{trans} [K] the translational temperature, x_{pert}, the mole fraction of the perturbers, and γ_{pert} [nm], the Van der Waals coefficients of each perturber for H_α [22].

$$\Delta\lambda_{Van\,der\,Waals}[nm] = \frac{p}{1\,atm}\left(\frac{273\,K}{T_{trans}}\right)^{0.7}\sum_{pert}\left(\frac{\gamma_{pert}}{100}x_{pert}\right) \qquad \text{Eq. 2}$$

In Eq. 2, the dominant mole fractions, x_{pert}, in an equilibrium CH_4-air flame are calculated at $\Phi = 0.8$. We used the CEA NASA code [51] at $T_{trans} = 2000$ K and $T_{trans} = 3000$ K, the limits of the plasma temperature in Section 4 and the Van der Waals coefficients, γ_{pert}, calculated in Table A3-A5 of Ref. [22]. Using the data of Table 2, the total Van der Waals HWHM calculated with Eq. 2 is equal to 0.007 nm at 2000 K, and 0.005 nm and 3000 K. We assume for simplicity that the Van der Waals HWHM is constant and equal to 0.006 nm.

The Stark HWHMs are calculated with Eq. 3, where n_e is the electron number density and $\Delta\lambda_{H_\alpha}$ the HWHM of the H_α line [54,55].

$$\frac{n_e}{10^{17}\text{cm}^{-3}} = \left(\frac{\Delta\lambda_{\text{H}_\alpha}}{0.549\text{ nm}}\right)^{1.47134} \qquad \text{Eq. 3}$$

The estimated HWHMs of the various broadening mechanisms are summarized in Table 3 and compared to a Stark HWHM of 0.014 nm, corresponding to the lowest electron number density measured in this work ($n_e = 5\times10^{14}$ cm^{-3}).

Table 3 HWHM of the H_α line at $n_e = 5\times10^{14}$ cm^{-3} based on the composition of an atmospheric pressure CH_4 – air flame (Φ = 0.8) at 2000 and 3000 K.

T_{gas} (K)	Instrumental broadening (nm)	Resonance (nm)	Van der Waals (nm)	Doppler (nm)	Stark (nm)
2000	0.035	<0.001	0.007	0.011	0.014
3000		<0.001	0.005	0.013	

Figure 6 presents a typical fit of the H_α emission obtained by a convolution of:

(i) the instrumental broadening profile,
(ii) the Doppler Gaussian profile (HWHM = 0.012 nm), and
(iii) the Van der Waals and Stark broadenings, simulated using a single Lorentzian profile.

The Lorentzian HWHM is varied until the simulated line agrees with the data. The Stark HWHM is finally obtained by subtracting the Van der Waals HWHM (0.006 nm) from the total Lorentzian HWHM. The error in the Stark width determination is estimated to be ± 15% (see Figure 6). The uncertainty in the electron number density measurement is ± 20%.

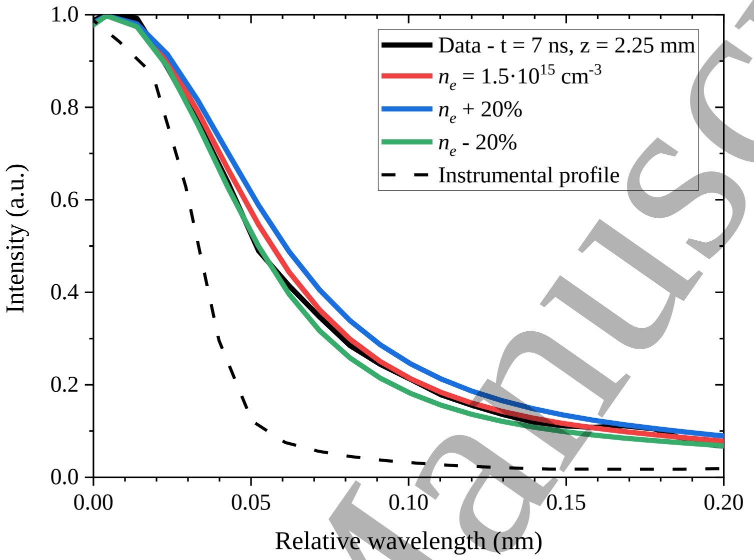

Figure 6 Fit of the H_α emission line at t = 7 ns, z = 2.25 mm, under the PASTEC conditions (Φ = 0.8, f = 20 kHz, E^p = 1.8 mJ). The wavelength is relative to the H_α line center. The error on the electron number density estimation is 20%. The dashed line represents the instrumental function.

The spectra of H_α are collected at various distances z from the cathode. The resulting distribution of the electron number density at several instants is shown in Figure 7. The initial electron distribution is relatively homogeneous along the gap, $n_e(t = 2\text{ ns}) \approx 10^{15}$ cm^{-3}, and is typical of sparks. During the applied pulse, n_e increases up to $3\cdot10^{15}$ cm^{-3} in the middle of the gap. In previous experiments on Mini-PAC with a propane-air flame, Pilla [31] obtained an electron number density of 10^{15} cm^{-3} at the same location, albeit his conditions were slightly different (propane flame of 25 kW, 10 kHz, 2.5-mJ pulses). The ionization degree is higher near the electrodes where, at the end of the pulse, n_e reaches about 10^{16} cm^{-3}. This electron number density at 1 bar and 3000 K corresponds to an ionization degree of ~ 1%.

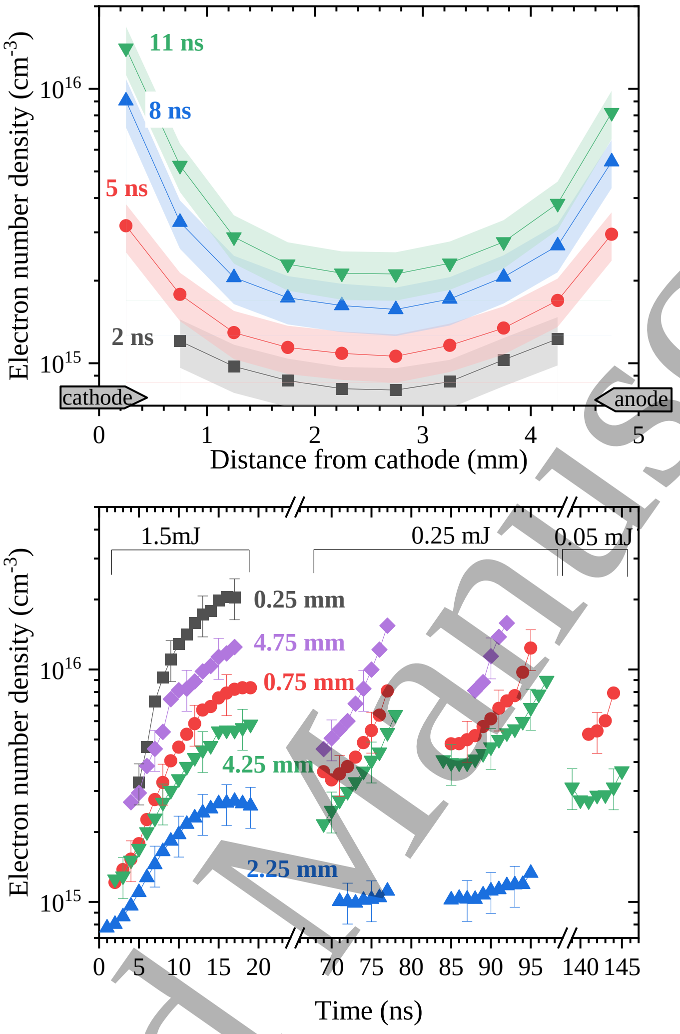

Figure 7 ***Top*****: Spatial distribution of the measured electron number density at *t* = 2, 5, 8, and 11 ns. The interelectrode distance is 5 mm.** ***Bottom*****: Temporal evolution of the electron number density at *z* = 0.25, 0.75, 2.25, 4.25, and 4.75 mm. The energy deposited by the pulses is given above the brackets. PASTEC conditions (Φ = 0.8, *f* = 20 kHz, E^p= 1.8 mJ.).**

Figure 7 shows the electron density profiles during the sequence of four pulses identified in Section 4. As stated before, the increase in n_e is faster close to the electrodes. At t = 17 ns, a maximum of n_e (2×10^{16} cm^{-3}) is reached at the cathode. After this moment, the H_α emission drops rapidly and the decay of n_e can no longer be measured. The larger electron number density at z = 0.25 mm (near the cathode) leads to the intermittent formation of thermal sparks [22] confined in the cathode vicinity. To account for the shot-to-shot variability, a two-Lorentzian fit of the H_α line is performed in this spatial region. It provides, in average, a similar result as presented in Figure 7 (see also Chap. 8 in [32]).

At t ~ 69 ns, the 2nd pulse reaches the electrodes, and the H_α emission is visible again. During the period between the 1st and 2nd pulses, we measure a decrease of 50% in the electron number density. Then n_e rises during the 2nd pulse in the same manner as the 1st one: faster close to the electrodes. The same scenario repeats during the 3rd and 4th pulses. Note that approximately 1.50 mJ are spent for the initial ionization. Then, 0.25 mJ is deposited, which allows for keeping n_e above 10^{15} cm^{-3} during at least 150 ns.

6. Number density of electronic states

6.1. Spectra acquisition and fitting

Plasma chemistry in NRP discharges is largely driven by the electronically excited states of molecules [56,57]. For instance, in preheated air, it was demonstrated that the quenching of excited electronic states of N_2 was responsible for a temperature increase of about 1000 K and was mainly responsible for the dissociation of O_2 [16,24,58]. This mechanism is negligible in corona and glow NRP discharges [23]. As demonstrated in Section 4, the temperature increases dramatically, which is likely due to dissociative quenching processes as in air. The development of an ultra-fast heating mechanism in a burnt mixture is a complex task that requires the knowledge of electronically excited states' number density. Thus, in this section, the number densities of excited electronic states are measured by quantitative OES.

Spectral measurements of the plasma radiation in the 300 – 370 nm range are used to determine the densities of $N_2(C)$, OH(A), and NH(A) and their rotational and vibrational temperatures. The spectra are obtained with an instrumental HWHM of ~ 0.075 nm, which causes a slightly higher inaccuracy in temperature measurements as compared to those performed in Section 4. The emission spectra are fitted using Specair [36,37]. A typical fit of OH(A-X), N_2(C-B), and NH(A-X) is given in Figure 8.

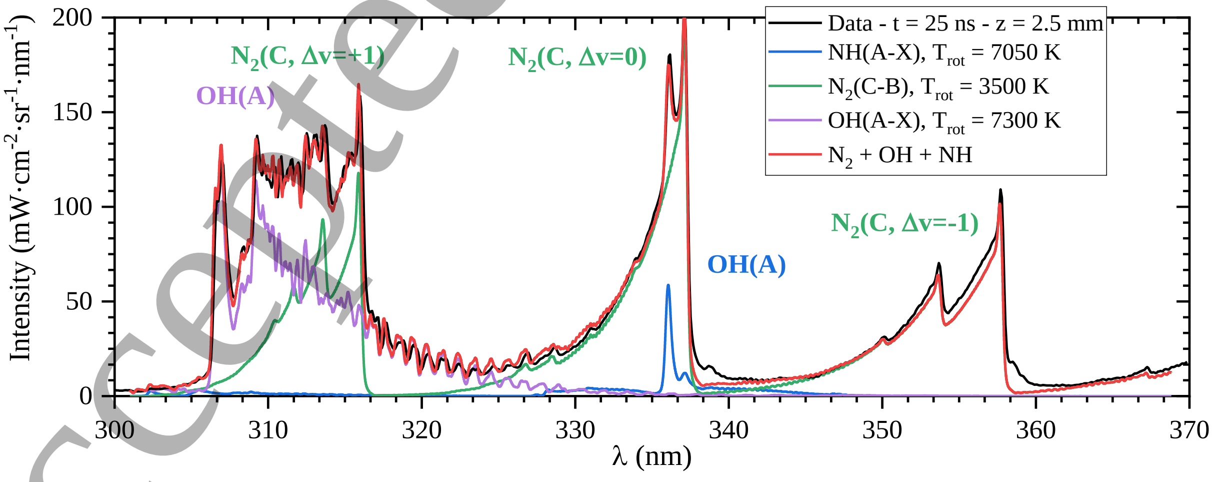

Figure 8 Typical fits of OH(A-X), N_2(C-B), and NH(A-X) emission spectra between 300 and 370 nm. The data are acquired under the PASTEC conditions (Φ = 0.8, f = 20 kHz, E^p= 1.8 mJ), t = 25 ns, and the emission is spatially averaged between

z = 2.25 and 2.75 mm (middle of the gap). The vibrational temperature of the synthetic spectra simulated with Specair is T_{vib} = 3950 K. The slight disagreement (below 5%) between 350 and 360 nm could be due to N_2^+(B-X) emission, not modeled here.

We find that T_{rot}[OH(A)] ranges between 6000 and 8000 K and that T_{rot}[NH(A]) ranges between 2000 and 9000 K. These values are higher than the translational temperature, thus the RT relaxation time of NH(A) and OH(A) is longer than their lifetime (for OH, RT relaxation time at 1 atm is approximately 20 ns [39]). The N_2(C) rotational temperatures agree within uncertainties with those obtained in Section 4. The vibrational temperatures of OH(A), N_2(C), and NH(A) are constant and uniform across the gap around T_{vib} = 4000 ± 500 K. These temperatures are not representative of the gas temperature, but rather of various excitation processes that change the vibrational population distribution.

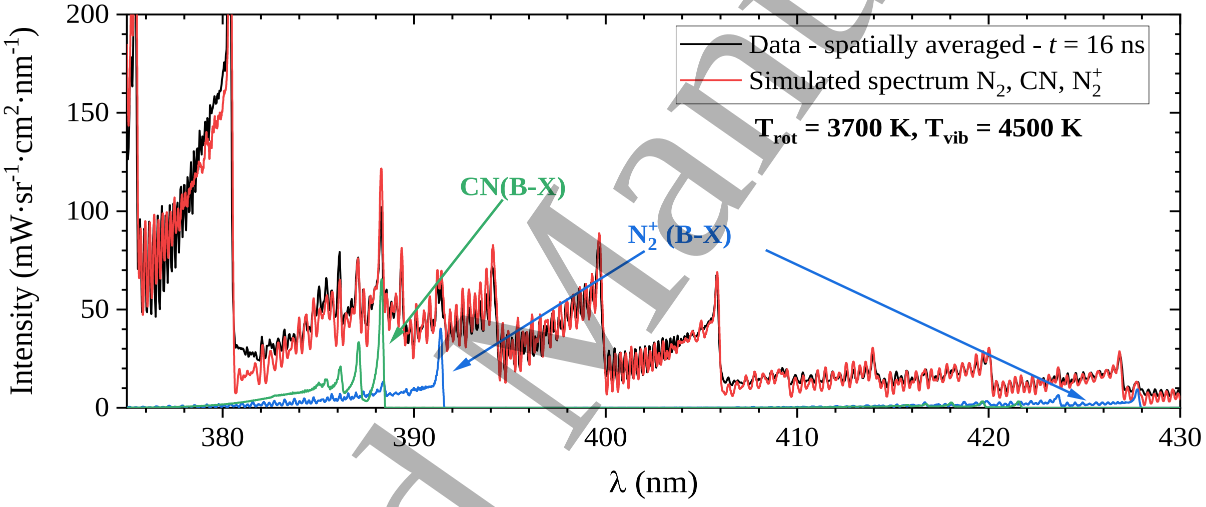

Figure 9 Calibrated spectrum (in black) compared with a simulated spectrum (in red) composed of N_2, CN, and N_2^+. The experimental spectrum is spatially averaged and measured at *t* = 16 ns under the PASTEC conditions (Φ = 0.8, *f* = 20 kHz, E^p = 1.8 mJ). The Specair spectra are simulated with T_{vib} = 4500 K and T_{rot} = 3700 K.

In the wavelength range 300 – 500 nm, the emission is dominated by the second positive system of N_2. However, for t ≥ 12 ns, other features can be detected such as CN violet emission, i.e. CN(B-X), and N_2^+ first negative system, i.e. N_2^+(B-X). In Figure 9, the emission spectra of these three species are simulated and compared with the spatially averaged spectrum acquired at *t* = 16 ns. In this case, we assumed all species have the same rotational and vibrational temperatures (T_{rot} = 3700 K and T_{vib} = 4500 K).

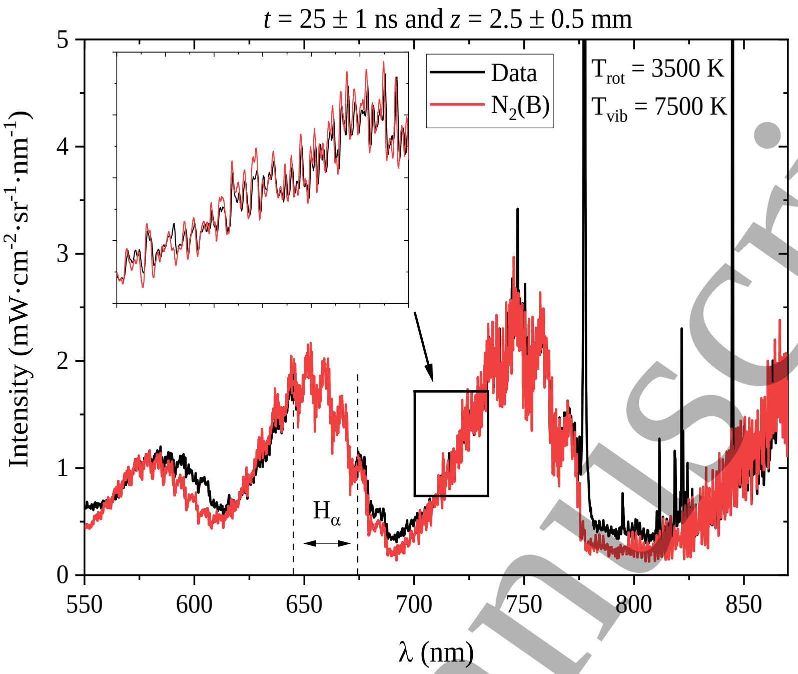

Figure 10 $N_2(B)$ emission at t = 25 ns and at z = 2.5 mm under the PASTEC conditions (Φ = 0.8, f = 20 kHz, E^p= 1.8 mJ). The synthetic spectrum is generated with Specair at T_{rot} = 3500 K and T_{vib} = 7500 K. No experimental data are acquired in the range 645 – 675 nm range to avoid CCD saturation by the H_α line.

Another set of experiments was also performed between 550 and 870 nm to acquire the $N_2(B\text{-}A)$ spectrum. The normalized emission is compared[2] to synthetic spectra of $N_2(B\text{-}A)$, varying T_{rot} and T_{vib}. For $t > 10$ ns and at the cathode, the continuum and atomic emission cannot be neglected and we discarded these spectra. A typical example of an $N_2(B\text{-}A)$ spectrum fitted with a Specair [36,37] simulation is shown in Figure 10. The measured emission between 645 and 675 nm is not recorded due to the strong emission of the H_α line. The atomic emission in the range 750 – 870 nm is not fitted. Note that an improved fitting procedure of the $N_2(B\text{-}A)$ emission, including vibrational overpopulation and the continuum emission (less than 0.1 $mW\cdot cm^{-2}\cdot sr^{-1}\cdot nm^{-1}$ at 550 nm) provides more accurate fittings but does not significantly change the number densities or the temperatures, see Chap. 8 of [32].

---

[2] To by-pass the time-expensive generation of $N_2(B\text{-}A)$ spectra, we calculated a set of $N_2(B\text{-}A)$ emission spectra using Specair and stored the spectra using the RADIS Python package [73]. The spectra were calculated at T_{rot} = 2000, 2250, … 4250 K and at T_{vib} = 6000, 6500, … 9000 K. The accuracy of the fitting is therefore equal to ±250 K for T_{rot}, and ±500 K for T_{vib}. RADIS is freely available at https://github.com/radis/radis.

6.1. Number density profiles

Thanks to the several sets of OES measurements described above, we determined the spatial and temporal distribution of $N_2(B)$, $N_2(C)$, CN(B), $N_2^+(B)$, OH(A), and NH(A). The measurement of $N_2(C)$ number density obtained from two different bands in two separate experiments (Figure 8 and Figure 9) agrees remarkably well, within better than 5%.

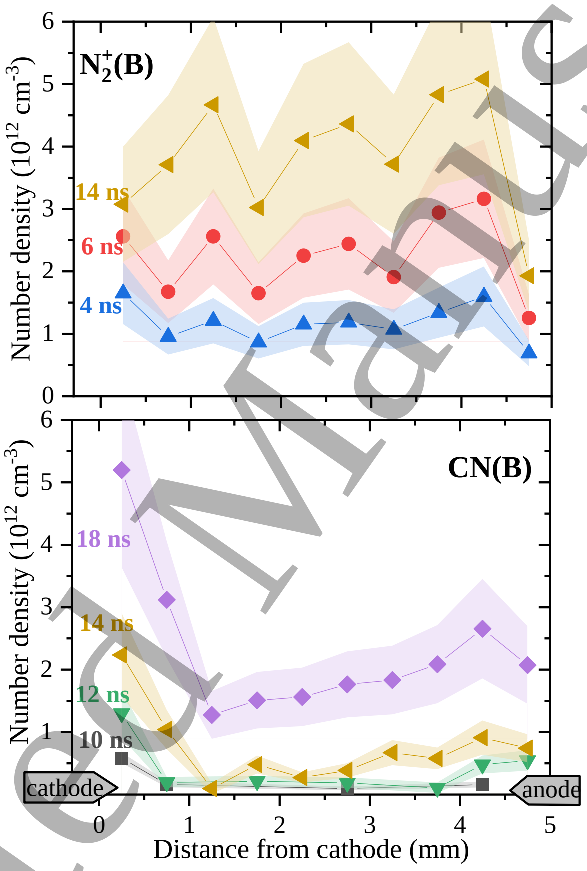

Figure 11 Distribution of the $N_2^+(B)$ and CN(B) number density along the interelectrode gap under the PASTEC conditions (Φ = 0.8, f = 20 kHz, E^p= 1.8 mJ.). Estimated error-bars are 30%, see Appendix B of [32]**. The measurements are optically averaged across ± 0.25 mm and the actual interelectrode distance is 5 mm.**

The number densities of CN(B) and $N_2^+(B)$ give an insight into the plasma chemistry during and after the pulse. Figure 11 shows the evolution of the CN(B) and $N_2^+(B)$ number density distributions along the interelectrode gap. By the end of the pulse, the CN number density increases in the entire gap. The effect is most pronounced at the cathode. The presence of atomic species near the electrode could significantly contribute to CN radical formation through the following reactions [59–61]:

$$C + N_2 \leftrightarrow CN + N \qquad \text{Reac.1}$$

$$CO + N \leftrightarrow CN + O \qquad \text{Reac.2}$$

For future work, confirmation of this CN formation mechanism deserves to be further analyzed in the case of NRP discharges applied to N_2:H_2O:CO_2 mixtures.

The ratio of N_2(C-B) and N_2^+(B-X) emission intensities can be used to determine the reduced electric field in air [62–64]. However, the coefficients relating the electric field to this ratio were determined by Paris *et al.* [62–64] only for air. To apply this method in the PASTEC conditions, precise knowledge of the N_2(C) and N_2^+(B) quenching rate coefficients by species such as CO_2 and H_2O is necessary. Therefore, with current knowledge of the plasma composition and quenching rate dependence with temperature, we cannot relate the N_2(C) and N_2^+(B) ratio to the electric field. However, the ratio of N_2(C) and N_2^+(B) number densities is relatively homogeneous along the interelectrode gap. Thus, the electric field is also expected to be homogeneous.

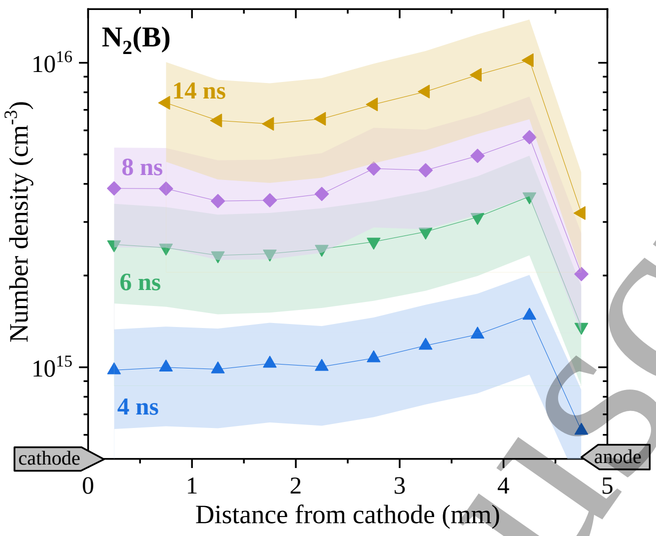

Figure 12 Distribution of $N_2(B)$ number density along the interelectrode gap from *t* = 4 ns to *t* = 14 ns. Estimated error-bars are 30%, see Appendix B of [32]. **PASTEC conditions (Φ = 0.8, *f* = 20 kHz, E^p= 1.8 mJ.).**

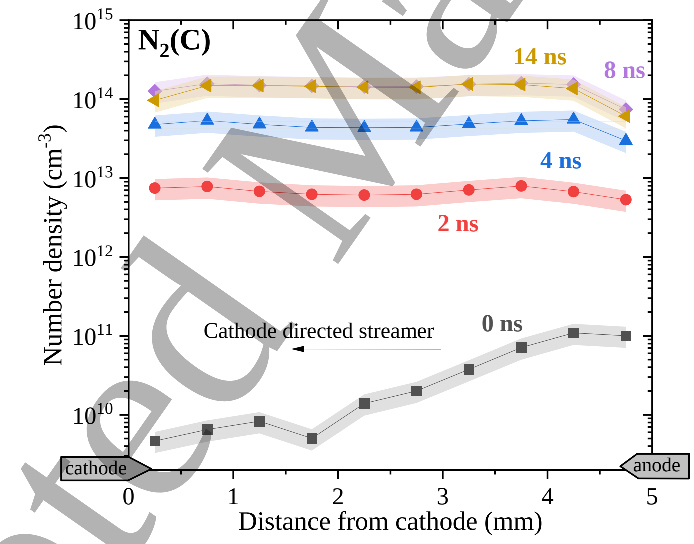

Figure 13 Distribution of $N_2(C)$ number density along the interelectrode gap from *t* = 0 ns to *t* = 14 ns and peaking at t = 10 ns. Estimated error-bars are 30%, see Appendix B of [32]. **PASTEC conditions (Φ = 0.8, *f* = 20 kHz, E^p= 1.8 mJ.).**

The distribution of $N_2(B)$ and $N_2(C)$ number densities extracted from calibrated spectra are shown in Figure 12 and Figure 13 for several instants. At *t* = 0 ns, the streamer propagation is captured, and the $N_2(C)$ number density varies from 10^{10} to 10^{11} cm^{-3} between anode and cathode. For $t \geq 2$ ns, the $N_2(C)$ distribution is relatively homogeneous (± 30%) along the discharge gap and increases from 10^{12} to 10^{14} cm^{-3} during the next 8 nanoseconds with the same uniformity. The $N_2(C)$ number density peaks at t = 10 ns, and then decreases. The number density of $N_2(B)$ is relatively peaked at the anode compared to the cathode (+50% at *t* = 14 ns). No reason can yet explain this gradient of $N_2(B)$ density. At its maximum, the total $N_2(B)$ number density is equal to 10^{16} cm^{-3}, which represents 0.5% of the total gas number density. The measurements close to the cathode could not be exploited for t > 8 ns due to atomic and continuum emission mixing with the N_2 first positive system.

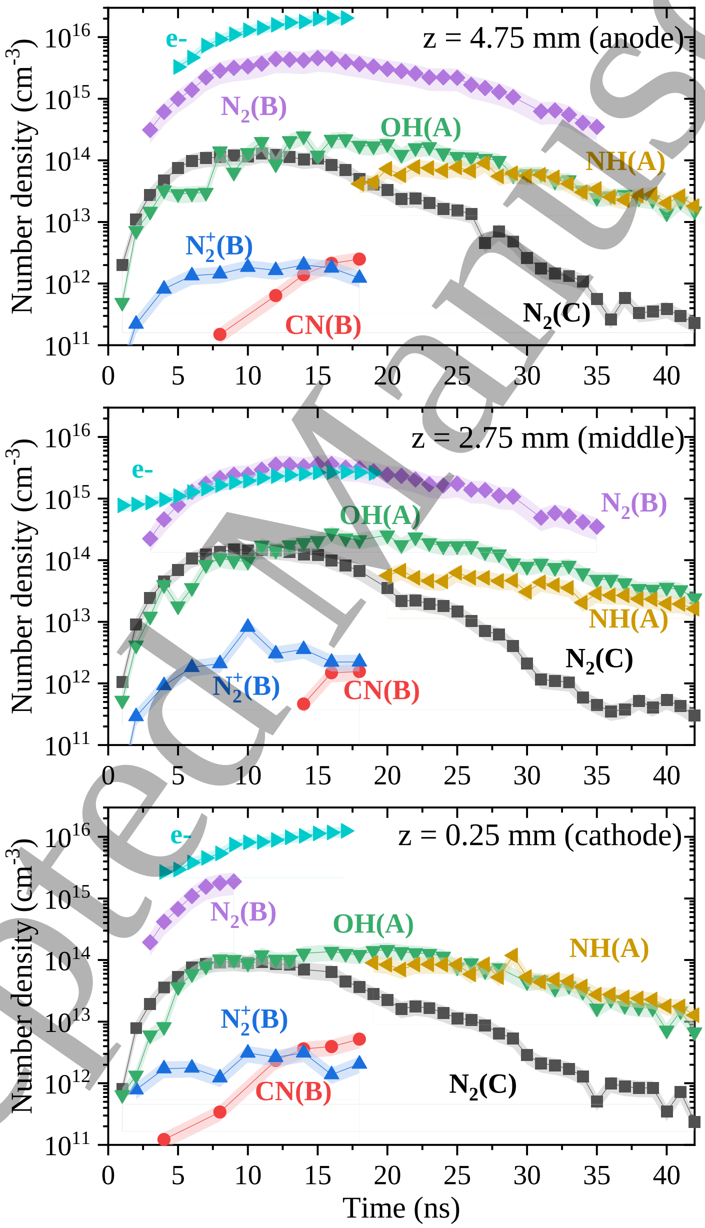

Figure 14 Evolution of the $N_2(B)$, $N_2(C)$, $OH(A)$, $NH(A)$, $N_2^+(B)$, and $CN(B)$ number densities under the PASTEC conditions ($\Phi = 0.8$, $f = 20$ kHz, $E^p = 1.8$ mJ.). The results are displayed at three locations: near the anode at z = 4.75 mm (top), in the

center of the interelectrode gap at z = 2.75 mm (middle), and near the cathode at z = 0.25 mm (bottom). For comparison, we also include the evolution of the electron number density.

In Figure 14, the number densities of $N_2(B)$, $N_2(C)$, OH(A), NH(A), $N_2^+(B)$, and CN(B) are plotted for locations near the electrodes and in the middle of the gap. The electron number density is added for comparison purposes. The number densities range from 10^{11} to 10^{16} cm^{-3}. As expected, the number densities of these excited states increase during the energy deposition (0 – 10 ns). Once the reduced electric field is turned off, the number density of species populated by electron impact such as $N_2(C)$ decreases. For the other species produced by other processes of energy transfer, such as CN(B) or OH(A), they reach their peak of number density at a later time. It is interesting to note that the number density of $N_2(B)$ is about 10-40 times higher than the density of $N_2(C)$. This ratio, obtained in the burnt gases, is similar to what was obtained for NRP discharges in pure air [24].

7. Conclusions

Energy measurements and quantitative OES were performed to provide an extensive characterization of NRP discharges applied in a burnt gases mixture. These results allow to identify the present discharge among the four types of NRP discharges: corona, glow, spark, and thermal spark [21,22]. Proper identification is essential as the chemical and physical properties of the NRP discharges vary dramatically from the NRP glow (*low ionization, no heating*) to the NRP thermal spark (*full ionization, thermal equilibrium*). In the present case, we observed that the discharge operates in the NRP spark regime (*intermediate ionization, substantial but limited heating*) with an average temperature increase of 550 K and an electron number density of 10^{15} – 10^{16} cm^{-3}.

In the example studied here, we characterized 1.8-mJ NRP spark discharges applied in the recirculation region of a lean premixed CH_4-air bluff-body stabilized flame. These results obtained at steady-state complement ongoing studies on the Mini-PAC burner at the EM2C laboratory and partners. We showed that the pulser creates a strong initial pulse of 1.5 mJ followed by 3 minor pulses, for a total deposited energy of 1.8 mJ in about 200 ns. We measured the gas temperature from the distribution of $N_2(C)$ rotational states. Initially, the plasma is approximately at ~ 2000 K near the electrodes and ~ 3000 K in the middle of the interelectrode gap. We found that, during the first pulse of 1.5 mJ, the temperature increase is three times higher near the electrodes. Approximately 20% of the electrical energy deposition is converted into heat. Finally, the number density evolution of several electronically excited species, namely $N_2(B)$, $N_2(C)$, $N_2^+(B)$, OH(A), NH(A), and CN(B), is measured by intensity-calibrated OES. The ratio of the densities of

N_2(B) and N_2(C) ranges between 10 and 40, which is close to what was found in preheated air [24] and shows that these discharges present similar plasma chemistry. These data are useful to validate detailed plasma chemistry calculations and, in a companion article (Part II), will be used to develop an analytical model for simulations of plasma-assisted combustion in a wide range of mixtures.

8. Acknowledgments

This work was partially funded by the ANR grant PASTEC ANR16-CE22-0005. Dr. Nicolas Minesi was supported by the IDEX Ph.D. fellowship ANR-11-IDEX-003-02. The authors would like to thank Sergey Stepanyan and Jean-Baptiste Perrin-Terrin for the energy and the time they invested in the preliminary work of these experiments, the CORIA laboratory for building the new Mini-PAC burner and for useful discussions on the experiment, Dr. Axel Vincent-Randonnier for helpful comments on this manuscript, Yannick Le Teno and Erika Jean-Bart for their technical support, and Cécile Oriot for the Mini-PAC photographs.

9. Appendix: Effect of probe location on voltage and current traces

A rigorous determination of the discharge electrical characteristics is necessary to ensure the reproducibility of the experiments as switching between NRP discharge regimes is highly sensitive to voltage [21]. The voltage and current of the discharge can be measured by attaching probes directly on the high voltage electrodes. This *direct configuration* was used in previous work at the EM2C laboratory and gave satisfactory results [11,21,24,65,66]. However, the probes occupy a significant volume around the discharge, which is not always compatible with optical diagnostics. Also, for practical applications in combustion, NRP discharges are used in harsh environments that typical probes cannot resist. Therefore, in our recent work, the voltage and current probes were positioned halfway in the coaxial cable delivering the high voltage [13,22,45,48,67]. This *remote configuration* solves the problems mentioned above and is found to provide additional information for plasma monitoring. The demonstration of the equivalence of the two methods is provided in this appendix.

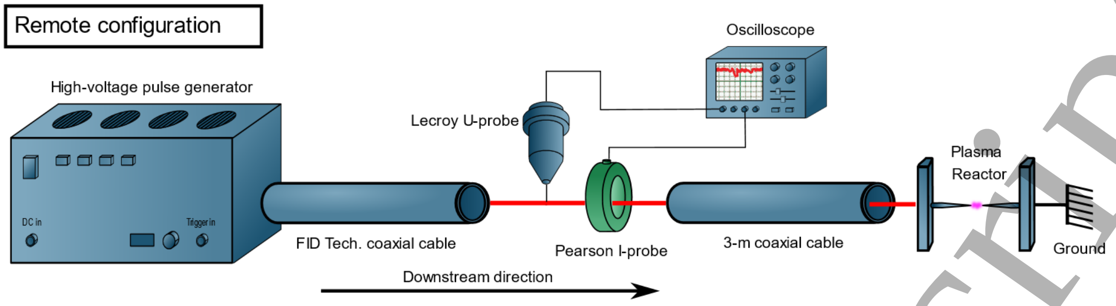

Figure 15 Remote configuration for current and voltage measurements. The current and voltage probes are close enough (< 2 cm) to assume they are simultaneous relative to the pulse duration. The core of the coaxial cables, represented in red, connects the pulser to the plasma reactor. The impedance mismatch between the cables (75 Ω) and the plasma induces reflections going in the upstream direction. In the setup presented in Figure 2, the "3-m coaxial cable" is removed.

The results of this section are performed at steady state in the PASTEC conditions. Incident pulses of 3.5 kV are generated at 20 kHz and delivered to the anode through a 6-m, 75-Ω coaxial cable. The voltage and current probes are placed either (i) in the middle of the 6-m cable or (ii) at the electrode. The experimental setup of (i) is shown in Figure 15. The voltage, current, and deposited energy measured at steady state are shown in Figure 16 for the two positions of the probes. For the considered steady-state regime at 20 kHz, the total deposited energy is 1.8 mJ per pulse. It can be seen in Figure 16 a) that an incident pulse of 2.2 mJ is generated and that only 1.5 mJ are deposited at the first passage. The remaining 0.7 mJ are reflected back toward the pulser. As described in Section 3, several additional pulses deliver more energy to the plasma and the measured total energy is practically the same for both probe configurations (1.80 mJ *versus* 1.85 mJ).

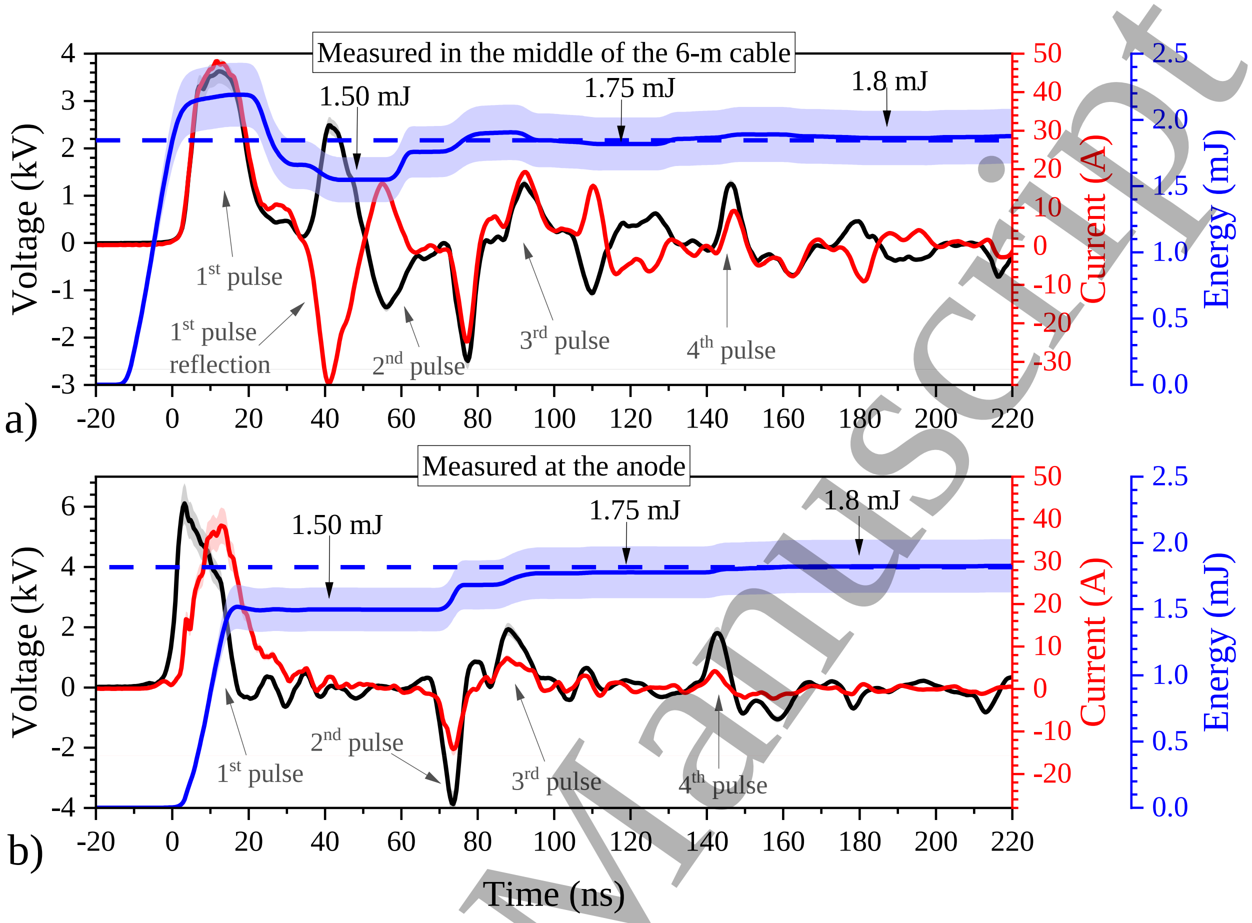

Figure 16 Voltage (black) and current (red) measured a) in the middle of a 6-m cable connecting the generator and the electrodes or b) at the electrode. The energy deposited in the plasma is obtained by integrating the product of the voltage and the current (the light swaths indicate the standard deviation).

Here we explain the difference in the voltage measured between Figure 16 a) and b). It is typically assumed that the “length” of an electrical waveform is large compared to the electrical circuitry. When using nanosecond discharges, it is not the case. In the coaxial cables of the present work, the pulses propagate at speed $c_{coax} = 2.0\times10^{8}$ m.s^{-1}. Thus, a 10-ns pulse spreads over a length of 2 m which is smaller than the cable coaxial length presented in Figure 15. Therefore, using a 3-m remote configuration, the nanosecond pulse is measured before any interaction with the electrodes. Following the schematic in Figure 15, the high-voltage pulse is generated by the pulser and propagates through a coaxial cable in the downstream direction. Then, the pulse travels through the voltage and the current probes. This order (i.e. current probe downstream of the voltage probe) is essential to properly account for the current leak in the voltage probe, see App. D of [68]. Finally, the pulse reaches the plasma reactor, is reflected in the upstream direction, and is measured again by the probes. The amplitude of the reflection, U_r, is related in Eq. 4 to the incident voltage amplitude

U_i, the plasma impedance, Z_{plasma} and the cable impedance Z_0 [69,70]. The voltage measured at the electrode is the sum of U_r and U_i, Eq. 5.

$$U_r = \frac{Z_{plasma} - Z_0}{Z_{plasma} + Z_0} U_i \qquad \text{Eq. 4}$$

$$U_{plasma} = U_r + U_i = \frac{2\,Z_{plasma}}{Z_{plasma} + Z_0} U_i \qquad \text{Eq. 5}$$

During the first picoseconds of the discharge, no electron has bridged the interelectrode gap and $Z_{plasma} \gg Z_0$. Thus, $U_{plasma} = 2U_i$ which explains why the maximum recorded voltage at the electrode (6 kV) is higher than the incident one (3.5 kV). After a few nanoseconds, depending on the ionization degree, Z_{plasma} becomes smaller than Z_0, the reflected pulse is of opposite polarity compared to the incident, and U_{plasma} decreases.

The remote measurement of the energy deposition allows to track the average plasma impedance and hence the average ionization fraction [69,71]. Assuming the plasma to be a homogeneous cylinder between two pins, the impedance of the plasma can be written [72] as:

$$Z_{plasma} = \frac{L}{S\sigma_{plasma}} \qquad \text{Eq. 6}$$

$$\sigma_{plasma} = \frac{n_e e^2}{m_e \nu_c} \qquad \text{Eq. 7}$$

where L is the length of the plasma between the two electrodes, S the cross-section of the plasma, n_e the electron number density, ν_c, the electron-heavy collision frequency, m_e the electron mass, and e the electron charge. For a weakly ionized plasma, the electron-heavy collision frequency can be expressed as:

$$\nu_c = N\sigma_n v \qquad \text{Eq. 8}$$

where, N is the total gas density, σ_n the cross-section of electron-neutral collision and v the mean thermal speed of the electrons, which can be expressed as:

$$v = \sqrt{\frac{8k_b T_e}{\pi m_e}} = \frac{T_e[\text{eV}]}{1.24} \times 10^7\ \text{cm}\cdot\text{s}^{-1} \qquad \text{Eq. 9}$$

Finally, the ionization fraction is:

$$\frac{n_e}{N} = \frac{\sigma_{plasma} m_e}{\text{e}^2}\ \sigma_n v \qquad \text{Eq. 10}$$

which can be simplified as follows:

$$\frac{n_e}{N} = 2.85 \times 10^{10} \frac{T_e[\mathrm{eV}]}{Z_{plasma}[\Omega]} \frac{L}{S}[\mathrm{cm}]\ \sigma_n[\mathrm{cm}^2] \qquad \text{Eq. 11}$$

In Figure 16 b), at t = 27 ns, the reflected voltage is close to zero, which indicates that the plasma impedance is close to the cable impedance[3] (75 Ω) at t = 12 ns. The optical diameter of the discharge is approximately 1 mm and we assume T_e ~ 1 eV. Applying Eq. 11, we get an ionization fraction of 4% at t = 12 ns, which corresponds[4] to the order of magnitude measured here.

10. References

[1] Starikovskaia S M 2014 Plasma-assisted ignition and combustion: nanosecond discharges and development of kinetic mechanisms *J. Phys. D. Appl. Phys.* **47** 353001

[2] Ju Y and Sun W 2015 Plasma assisted combustion: Dynamics and chemistry *Prog. Energy Combust. Sci.* **48** 21–83

[3] Popov N A 2016 Kinetics of plasma-assisted combustion: effect of non-equilibrium excitation on the ignition and oxidation of combustible mixtures *Plasma Sources Sci. Technol.* **25** 043002

[4] Vincent-Randonnier A 2010 Combustion Enhancement and Stabilization: Principles of Plasma Assistance and Diagnostics Tools *Handbook of Combustion* vol 5 (Weinheim, Germany: Wiley-VCH Verlag GmbH & Co. KGaA)

[5] Vincent-Randonnier A, Larigaldie S, Magre P and Sabel'nikov V 2007 Plasma assisted combustion: effect of a coaxial DBD on a methane diffusion flame *Plasma Sources Sci. Technol.* **16** 149–60

[6] Mao X, Chen Q and Guo C 2019 Methane pyrolysis with N2/Ar/He diluents in a repetitively-pulsed nanosecond discharge: Kinetics development for plasma assisted combustion and fuel reforming *Energy Convers. Manag.* **200** 112018

[7] Zhong H, Mao X, Rousso A C, Patrick C L, Yan C, Xu W, Chen Q, Wysocki G and Ju Y 2021 Kinetic study of plasma-assisted n-dodecane/O2/N2 pyrolysis and oxidation in a nanosecond-pulsed

---

[3] The electrical measurements performed upstream of the discharge are delayed by 15 ns. Therefore, the measurements acquired at t = 27 ns correspond to events occurring at t = 12 ns.

[4] Eq. 11 is applicable for homogeneous plasmas. For a more accurate use of this technique, inhomogeneities of the plasma (e.g. the cathode and anode sheaths) must be considered. Also, at such ionization fractions, electron-ion collisions should be considered [71].

discharge *Proc. Combust. Inst.* **38** 6521–31

[8] Kim W, Mungal M G and Cappelli M A 2008 Formation and role of cool flames in plasma-assisted premixed combustion *Appl. Phys. Lett.* **92** 2006–9

[9] Shcherbanev S, Morinière T, Solana-Pérez R, Weilenmann M, Xiong Y, Doll U and Noiray N 2020 Anchoring of premixed jet flames in vitiated crossflow with pulsed nanosecond spark discharge *Appl. Energy Combust. Sci.* **1–4** 100010

[10] Dunn I, Ahmed K A, Leiweke R J and Ombrello T M 2021 Optimization of flame kernel ignition and evolution induced by modulated nanosecond-pulsed high-frequency discharge *Proc. Combust. Inst.* **38** 6541–50

[11] Pilla G, Galley D, Lacoste D A, Lacas F, Veynante D and Laux C O 2006 Stabilization of a Turbulent Premixed Flame Using a Nanosecond Repetitively Pulsed Plasma *IEEE Trans. Plasma Sci.* **34** 2471–7

[12] Barbosa S, Pilla G, Lacoste D A, Scouflaire P, Ducruix S, Laux C O and Veynante D 2015 Influence of nanosecond repetitively pulsed discharges on the stability of a swirled propane/air burner representative of an aeronautical combustor *Philos. Trans. R. Soc. A Math. Phys. Eng. Sci.* **373** 20140335

[13] Vignat G, Minesi N, Soundararajan P R, Durox D, Renaud A, Blanchard V, Laux C O and Candel S 2021 Improvement of lean blow out performance of spray and premixed swirled flames using nanosecond repetitively pulsed discharges *Proc. Combust. Inst.* **38** 6559–66

[14] Xu D A, Shneider M N, Lacoste D A and Laux C O 2014 Thermal and hydrodynamic effects of nanosecond discharges in atmospheric pressure air *J. Phys. D. Appl. Phys.* **47** 235202

[15] Lacoste D A, Moeck J P, Durox D, Laux C O and Schuller T 2013 Effect of Nanosecond Repetitively Pulsed Discharges on the Dynamics of a Swirl-Stabilized Lean Premixed Flame *J. Eng. Gas Turbines Power* **135** 101501

[16] Popov N A 2016 Pulsed nanosecond discharge in air at high specific deposited energy: Fast gas heating and active particle production *Plasma Sources Sci. Technol.* **25** 44003

[17] Bak M S and Cappelli M A 2015 A reduced set of air plasma reactions for nanosecond pulsed plasmas *IEEE Trans. Plasma Sci.* **43** 995–1001

[18] Aleksandrov N L, Kindysheva S V, Nudnova M M and Starikovskiy A Y 2010 Mechanism of ultra-fast heating in a non-equilibrium weakly ionized air discharge plasma in high electric fields *J. Phys.*

D. Appl. Phys. **43** 255201

[19] Castela M, Fiorina B, Coussement A, Gicquel O, Darabiha N and Laux C O 2016 Modelling the impact of non-equilibrium discharges on reactive mixtures for simulations of plasma-assisted ignition in turbulent flows *Combust. Flame* **166** 133–47

[20] Bechane Y and Fiorina B 2021 Numerical investigations of turbulent premixed flame ignition by a series of Nanosecond Repetitively Pulsed discharges *Proc. Combust. Inst.* **38** 6575–82

[21] Pai D Z, Lacoste D A and Laux C O 2010 Transitions between corona, glow, and spark regimes of nanosecond repetitively pulsed discharges in air at atmospheric pressure *J. Appl. Phys.* **107** 093303

[22] Minesi N, Stepanyan S, Mariotto P, Stancu G D and Laux C O 2020 Fully ionized nanosecond discharges in air: the thermal spark *Plasma Sources Sci. Technol.* **29** 85003

[23] Pai D Z, Stancu G D, Lacoste D A and Laux C O 2009 Nanosecond repetitively pulsed discharges in air at atmospheric pressure - The glow regime *Plasma Sources Sci. Technol.* **18** 045030

[24] Rusterholtz D L, Lacoste D A, Stancu G D, Pai D Z and Laux C O 2013 Ultrafast heating and oxygen dissociation in atmospheric pressure air by nanosecond repetitively pulsed discharges *J. Phys. D. Appl. Phys.* **46** 464010

[25] Minesi N, Mariotto P, Pannier E, Stancu G D and Laux C O 2021 The role of excited electronic states in ambient air ionization by a nanosecond discharge *Plasma Sources Sci. Technol.* **30** 035008

[26] Yong T, Abdalla A I and Cappelli M A 2021 Laser absorption measurements of electron density in nanosecond-scale atmospheric pressure pulsed plasmas *Phys. Plasmas* **28** 053501

[27] Pai D Z, Lacoste D A and Laux C O 2010 Nanosecond repetitively pulsed discharges in air at atmospheric pressure-the spark regime *Plasma Sources Sci. Technol.* **19** 065015

[28] Lacoste D A, Moeck J P, Roberts W L, Chung S H and Cha M S 2017 Analysis of the step responses of laminar premixed flames to forcing by non-thermal plasma *Proc. Combust. Inst.* **36** 4145–53

[29] DI Sabatino F, Guiberti T F, Moeck J P, Roberts W L and Lacoste D A 2021 Actuation efficiency of nanosecond repetitively pulsed discharges for plasma-assisted swirl flames at pressures up to 3 bar *J. Phys. D. Appl. Phys.* **54**

[30] Bonebrake J M, Blunck D L, Lefkowitz J K and Ombrello T M 2019 The effect of nanosecond pulsed high frequency discharges on the temperature evolution of ignition kernels *Proc. Combust. Inst.* **37** 5561–8

[31] Pilla G 2008 *Etude Expérimentale de la Stabilisation de Flammes Propane-Air de Prémélange par*

Décharges Nanosecondes Impulsionnelles Répétitives (Ecole Centrale Paris, PhD Thesis, in French)

[32] Minesi N 2020 *Thermal spark formation and plasma-assisted combustion by nanosecond repetitive discharges* (Université Paris-Saclay, PhD Thesis)

[33] Perrin-Terrin J 2020 *Rapport "Parcours recherche" - CentraleSupélec - 2ème année (in French)*

[34] Lepikhin N D, Popov N A and Starikovskaia S M 2018 Fast gas heating and radial distribution of active species in nanosecond capillary discharge in pure nitrogen and N2:O2 mixtures *Plasma Sources Sci. Technol.* **27**

[35] Lo A, Cessou A, Boubert P and Vervisch P 2014 Space and time analysis of the nanosecond scale discharges in atmospheric pressure air: I. Gas temperature and vibrational distribution function of N $_2$ and O $_2$ *J. Phys. D. Appl. Phys.* **47** 115201

[36] Specair 2012 Specair 3.0 *http://www.spectralfit.com*

[37] Laux C O, Spence T G, Kruger C H and Zare R N 2003 Optical diagnostics of atmospheric pressure air plasmas *Plasma Sources Sci. Technol.* **12** 125–138

[38] Popov N A 2011 Kinetic processes initiated by a nanosecond high-current discharge in hot air *Plasma Phys. Reports* **37** 807–15

[39] Bruggeman P J, Sadeghi N, Schram D C and Linss V 2014 Gas temperature determination from rotational lines in non-equilibrium plasmas: a review *Plasma Sources Sci. Technol.* **23** 23001

[40] Olsen H L, Edmonson R B and Gayhart E L 1952 Microchronometric Schlieren Study of Gaseous Expansion from an Electric Spark *J. Appl. Phys.* **23** 1157–62

[41] Kono M, Niu K, Tsukamoto T and Ujiie Y 1989 Mechanism of flame kernel formation produced by short duration sparks *Symp. Combust.* **22** 1643–9

[42] Albrecht H, Bloss W H, Herden W H, Maly R, Saggau B and Wagner E 1977 New Aspects on Spark Ignition *SAE Tech. Pap.* 770853

[43] Stepanyan S, Hayashi J, Salmon A, Stancu G D and Laux C O 2017 Large-volume excitation of air, argon, nitrogen and combustible mixtures by thermal jets produced by nanosecond spark discharges *Plasma Sources Sci. Technol.* **26** 22–4

[44] Castela M, Stepanyan S, Fiorina B, Coussement A, Gicquel O, Darabiha N and Laux C O 2017 A 3-D DNS and experimental study of the effect of the recirculating flow pattern inside a reactive kernel produced by nanosecond plasma discharges in a methane-air mixture *Proc. Combust. Inst.* **36** 4095–103

[45] Stepanyan S, Minesi N, Tibère-Inglesse A, Salmon A, Stancu G D and Laux C O 2019 Spatial evolution of the plasma kernel produced by nanosecond discharges in air *J. Phys. D. Appl. Phys.* **52** 295203

[46] Orriere T 2018 *Confinement micrométrique des décharges pulsées nanosecondes dans l'air à pression atmosphérique et effets électro-aérodynamiques* (Université de Poitiers, PhD Thesis, in French)

[47] Lo A, Cessou A and Vervisch P 2014 Space and time analysis of the nanosecond scale discharges in atmospheric pressure air: II. Energy transfers during the post-discharge *J. Phys. D. Appl. Phys.* **47** 115202

[48] Dumitrache C, Gallant A, Minesi N, Stepanyan S, Stancu G D and Laux C O 2019 Hydrodynamic regimes induced by nanosecond pulsed discharges in air: mechanism of vorticity generation *J. Phys. D. Appl. Phys.* **52** 364001

[49] Popov N A 2001 Investigation of the mechanism for rapid heating of nitrogen and air in gas discharges *Plasma Phys. Reports* **27** 886–96

[50] Flitti A and Pancheshnyi S 2009 Gas heating in fast pulsed discharges in N 2 –O 2 mixtures *Eur. Phys. J. Appl. Phys.* **45** 21001

[51] McBride B J and Gordon S 1992 Computer program for calculating and fitting thermodynamic functions

[52] Griem H R 1974 *Spectral Line Broadening by Plasmas* (New York: ACADEMIC PRESS, INC.)

[53] Lamoureux N, Foo K K and Desgroux P 2021 Quantitative measurement of atomic hydrogen in low-pressure methane flames using two-photon LIF calibrated by krypton *Combust. Flame* **224** 248–59

[54] Gigosos M A, González M Á and Cardeñoso V 2003 Computer simulated Balmer-alpha, -beta and -gamma Stark line profiles for non-equilibrium plasmas diagnostics *Spectrochim. Acta - Part B At. Spectrosc.* **58** 1489–504

[55] Konjević N, Ivković M and Sakan N 2012 Hydrogen Balmer lines for low electron number density plasma diagnostics *Spectrochim. Acta Part B At. Spectrosc.* **76** 16–26

[56] Kossyi I A, Kostinsky A Y, Matveyev A A and Silakov V P 1992 Kinetic scheme of the non-equilibrium discharge in nitrogen-oxygen mixtures *Plasma Sources Sci. Technol.* **1** 207–20

[57] Capitelli M, Bruno D and Laricchiuta A 2013 *Fundamental Aspects of Plasma Chemical Physics*

Transport vol 85 (New York, NY: Springer New York)

[58] Stancu G D, Kaddouri F, Lacoste D A and Laux C O 2010 Atmospheric pressure plasma diagnostics by OES, CRDS and TALIF *J. Phys. D. Appl. Phys.* **43** 124002

[59] Martin A, Boyd I D, Cozmuta I and Wright M J 2010 Chemistry model for ablating carbon-phenolic material during atmospheric re-entry *48th AIAA Aerosp. Sci. Meet. Incl. New Horizons Forum Aerosp. Expo.* 2010–1175

[60] Gökçen T 2007 N2 - CH4 - Ar chemical kinetic model for simulations of titan atmospheric entry *J. Thermophys. Heat Transf.* **21** 9–18

[61] Magin T E, Caillault L, Bourdon A and Laux C O 2006 Nonequilibrium radiative heat flux modeling for the Huygens entry probe *J. Geophys. Res.* **111** E07S12

[62] Paris P, Aints M, Valk F, Plank T, Haljaste A, Kozlov K V and Wagner H-E 2005 Intensity ratio of spectral bands of nitrogen as a measure of electric field strength in plasmas *J. Phys. D. Appl. Phys.* **38** 3894–9

[63] Paris P, Aints M, Valk F, Plank T, Haljaste A, Kozlov K V and Wagner H-E 2006 Reply to comments on 'Intensity ratio of spectral bands of nitrogen as a measure of electric field strength in plasmas' *J. Phys. D. Appl. Phys.* **39** 2636–9

[64] Pancheshnyi S 2006 Comments on 'Intensity ratio of spectral bands of nitrogen as a measure of electric field strength in plasmas' *J. Phys. D. Appl. Phys.* **39** 1708–10

[65] Sainct F P, Lacoste D A, Kirkpatrick M J, Odic E and Laux C O 2014 Temporal evolution of temperature and OH density produced by nanosecond repetitively pulsed discharges in water vapour at atmospheric pressure *J. Phys. D. Appl. Phys.* **47** 75204

[66] Xu D A, Lacoste D A, Rusterholtz D L, Elias P-Q, Stancu G D and Laux C O 2011 Experimental study of the hydrodynamic expansion following a nanosecond repetitively pulsed discharge in air *Cit. Appl. Phys. Lett* **99**

[67] Minesi N, Stepanyan S A, Mariotto P B, Stancu G-D and Laux C O 2019 On the arc transition mechanism in nanosecond air discharges *AIAA Scitech 2019 Forum* vol 2019 (Reston, Virginia: American Institute of Aeronautics and Astronautics) p 0463

[68] Pannier E 2019 *Conversion of carbon dioxyde with nanosecond repetitive discharges* (CentraleSupélec, PhD Thesis)

[69] Pai D Z 2008 *Nanosecond Repetitively Pulsed Plasmas in Preheated Air at Atmospheric Pressure*

(Ecole Centrale Paris, PhD Thesis)

[70] Martin S and Martin S 2018 Transmission and Propagation of Electromagnetic Waves *Modern Telecommunications* (Cambridge University Press) pp 103–30

[71] Orriere T, Moreau E and Pai D Z 2018 Ionization and recombination in nanosecond repetitively pulsed microplasmas in air at atmospheric pressure *J. Phys. D. Appl. Phys.* **51** 494002

[72] Raizer Y P 1991 *Gas Discharge Physics* ed J E Allen (Springer Verlag. Berlin.)

[73] Pannier E and Laux C O 2019 RADIS: A nonequilibrium line-by-line radiative code for CO2 and HITRAN-like database species *J. Quant. Spectrosc. Radiat. Transf.* **222**–**223** 12–25